In Workshop on Mathematical Methods in Biomedical Image Analysis (MMBIA)
p. 163-170, December 2001

Tumor-Induced Structural and Radiometric Asymmetry in Brain Images

Peter Lorenzen, Sarang Joshi, Guido Gerig, and Elizabeth Bullitt

Medical Image Display and Analysis Group, University of North Carolina at Chapel Hill, NC 27599

Abstract. This paper presents a general framework for analyzing structural and radiometric asymmetry in brain images. In a healthy brain, the left and right hemispheres are largely symmetric across the mid-sagittal plane. Brain tumors may belong to one or both of the following categories: mass-effect, in which the diseased tissue displaces healthy tissue; and infiltrating, in which healthy tissue has become diseased. Mass-effect brain tumors cause structural asymmetry by displacing healthy tissue, and may cause radiometric asymmetry in adjacent normal structures due to edema. Infiltrating tumors have a different radiometric response from healthy tissue. Thus, structural and radiometric asymmetries across the mid-sagittal plane in brain images provide important cues that tumors may be present. We have developed a framework that registers images with their reflections across the mid-sagittal plane. The registration process accounts for tissue displacement through large deformation image warping. Radiometric differences are taken into account through an additive intensity field. We present an efficient multi-scale algorithm for the joint estimation of structural and radiometric asymmetry.

Key Words: Brain symmetry analysis, plane of symmetry estimation, deformable image mapping, medical image analysis.

1 Introduction

The healthy human brain is largely symmetric across the mid-sagittal plane. Recognizing that structural asymmetry may indicate disease, in our previous work we examined shape and volume differences between the left and right hippocampi in patients with schizophrenia [1,2,3,4], epilepsy [5], and Alzheimer's disease [6]. Most other work involving structural asymmetry has focused on small-scale geometric inter-hemispheric differences [7,8,9,10,11,12,13]. Up to now, little attention has been paid to gross differences between the left and right brain hemispheres in patients with brain tumors. In this paper, we describe our unified framework for studying not only large- and small-scale structural variations, but also intensity variations occurring in images of patients with brain tumors.

As part of a larger effort aimed at improving the diagnosis and treatment of tumor patients, our group is investigating techniques for analyzing the regional effects and vascular characteristics of brain tumors. The initial stages of this work aim toward the automatic identification of tumors in MR images. We are investigating several, potentially synergistic, methods for segmenting tumors: multi-channel (white matter, grey matter, and cerebrospinal fluid) statistical pattern recognition, level set evolution, atlas-based registration, and asymmetry analysis.

Tumors exhibit two main effects in MR images: mass-effect and infiltration. Mass-effect tumors displace and distort the underlying structure. Infiltrating tumors affect the tissue characteristics, changing the radiometric response in the image. Most cases show a combination of these two effects. For example, in purely mass-effect tumors, the presence of edema induces changes in the radiometric response of adjacent normal structures. We have developed a single framework to study both structural and radiometric asymmetry in images of patients with brain tumors.

We study the asymmetry of the brain in MR images by registering an image with its reflection about the plane of symmetry. Given a scalar 3D MR image, $I(x) \in \mathbb{R}^+$ where $x = [x_1, x_2, x_3]^T \in \Omega \subset \mathbb{R}^3$, of the brain and corresponding plane of symmetry, the structural deformations and changes in the radiometric response of the tissue due to the the disease process are estimated via the following mean squared error minimization

$$\hat{H},\, \hat{q},\, \hat{d},\, \hat{f} = \arg \min_{H,\, q\, ,d,\, f} \int_{\Omega} ||I(x) - I(H(x-q)+q+d(x)) + f(x)||^2 dx \quad (1)$$

where H is a Householder reflection matrix and $q \in \mathbb{R}^3$ is a translation characterizing the plane of symmetry. The high dimensional vector field $d(x) \in \mathbb{R}^3$ describes the geometric deformations in the brain across the plane of symmetry, and the additive scalar intensity field $f(x) \in \mathbb{R}$ describes the intensity variation. The latter two quantities are regularized with deriva-

tive operators to ensure smoothness during the estimation process.

In this paper, we present a two-stage algorithm. In the first stage of the process, $\hat{H}, \hat{q}, \hat{f}$ are estimated through a multi-scale iterative approach while holding the deformation field fixed as the additive identity, $d(x) = 0, \forall x \in \Omega$. In this way, we obtain both the estimated plane of symmetry characterized by $\hat{H}$ and $\hat{q}$, and an initial estimate of the intensity variation field, $\hat{f}$.

The second stage estimates the structural deformations characterized by $d(x)$ in Equation (1) and refines the estimate of the intensity field variation $f(x)$ via an extension of the large deformation diffeomorphic image warping algorithms developed in [14,15,16].

This paper is divided into sections according to the two-stage process mentioned above. The following section (Section 2) develops the first part of the framework which involves estimating the plane of symmetry and initial intensity field variation. Section 3 extends the framework to include high dimensional local deformations. The remaining sections discuss the results and the performance of the algorithms.

2 Estimation of Plane of Symmetry

Given a scalar 3D MR image, $I(x)$, of the brain we would like to estimate the plane of symmetry as well as investigate the inter-hemispheric asymmetry in the brain. In this paper, we define the plane of symmetry to be the plane about which inter-hemispheric similarity is maximal. This plane is not necessarily the mid-sagittal plane defined by the *anterior commissure* and the *posterior commissure* [17].

A number of techniques have been employed to compute the plane of symmetry in MR images of the brain. Many of these methods involve fitting a 3D plane from a set of symmetry lines extracted from 2D images. Smith and Jenkinson [11] present an algorithm that finds symmetry via symmetry profiles. Of these 2D approaches many employ a cross-correlation symmetry measure. Liu et al. [18,19] extract the plane of symmetry from a set of 2D slices via an edge-based technique.

Our approach differs from these methods in that we make a direct estimation of the plane of symmetry from a whole 3D volume. This approach is less sensitive to the variability in the inter-hemispheric fissure. Ardekani [20] et al. present a 3D multi-resolution cross-correlation method for estimating the plane of symmetry. Prima et al [21] present an in-depth analysis of previous plane of symmetry estimation methods along with their own, which involves matching the centers of homologous blocks by reflective symmetry. Rather than performing a series of localized point-to-point correspondences, we estimate the plane of symmetry globally over all Ω. The plane of symmetry is parameterized via the Householder reflection matrix, H, and a translation, q. The inter-hemispheric intensity variation due to the presence of tumors or bias field induced by the MR acquisition or both is modeled as an additive scalar field $f(x)$.

The inter-hemispheric intensity variation due to the presence of tumors is modeled as an additive scalar Gaussian random field, $f(x)$, with covariance induced by a linear differential operator L_f following [22]. Namely, we let $\{f(x), x \in \Omega\}$ be a random process process satisfying the stochastic partial differential equation

$$L_f f(x) = e(x)$$

where $e(x)$ is white noise. That is, $\langle e, y\rangle \sim \mathcal{N}(0, \langle y, y\rangle)$. From [22] we know that $\{f(x), x \in \Omega\}$ is a zero-mean Gaussian process with covariance

$$K(x,y) = \int G(x,u)G(y,u)du,$$

where G is the Green's function of L_f satisfying $LG(x,y) = \delta(x-y)$. Since L_f is the Laplacian, ∇^2, $G(x,y) = \frac{1}{||x-y||}$.

Using the Bayesian paradigm the global energy function is defined using a Gaussian mean squared error data likelihood function and the quadratic Gaussian norm induced by the linear differential operator on $f(x)$. The linear differential operator norm enforces smoothness constraints and regularizes the estimation of the the additive intensity field. The optimization then becomes:

$$\hat{H}, \hat{q}, \hat{f} = \arg\min_{H,q,f} \int_\Omega ||I(x) - I(H(x-q)+q) + f(x))||^2 dx + \beta \int_\Omega ||L_f f(x)||^2 dx \quad (2)$$

where $L_f = \nabla^2$ is the Laplacian operator.

2.1 Algorithm for Estimating the Plane of Symmetry

We begin by defining the parameterization of the plane of symmetry via the Householder reflection matrix. We construct a reflection matrix H from a plane characterized by its unit normal vector v shown in Figure 1.

Let p' be the reflection of the point $p \in \Omega$ about the plane of symmetry. We let p_1 be the projection of p onto the line defined by v, that is $p_1 = vv^T p$. Let p_2

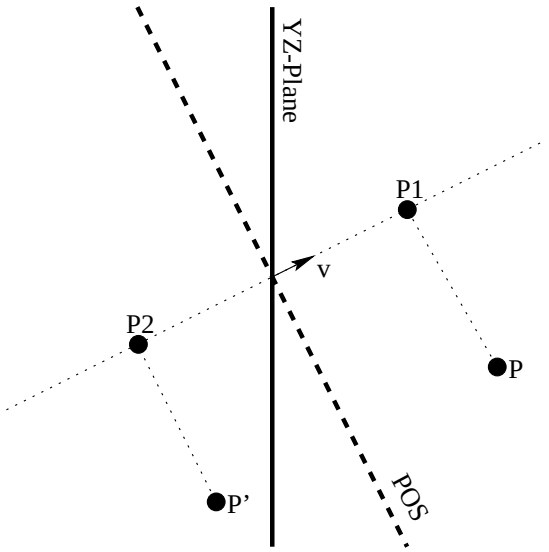

Fig. 1. This figure depicts the Householder reflection construction. The plane of symmetry, POS, is characterized by its normal, v.

be the reflection of p_1 about the origin, $p_2 = -p_1 = -vv^T p$. Therefore, $p' = p + p_2 - p_1$ and, hence, $Hp = Ip - vv^T p - vv^T p = (I - 2vv^T)p$. Thus, given a plane as described by v, we can construct its associated Householder reflection matrix,

$$H = I - 2vv^T, \tag{3}$$

where $||v|| = 1$ is the Householder vector. The Householder matrix is symmetric, $H^T = H$, and orthogonal, $H^T H = I$, with determinant $\det|H| = \det|I - 2vv^T| = 1 - 2||v||^2 = -1$.

In our framework an image, $I(x)$, is considered to have perfect symmetry about a plane defined by Householder reflection matrix H passing through point q if

$$\int_\Omega ||I(x) - I(H(x-q)+q)||^2 dx = 0.$$

The iterative algorithm for minimizing the energetics defined in Equation (2) is derived by embedding the optimization of the Householder matrix H and corresponding point q in the space of affine motions $GL(3) \times \mathbb{R}^3 \subset \mathbb{R}^{12}$. Rather than estimating $\hat{H}$ and $\hat{q}$ directly, we estimate an affine matrix, $\hat{A}$, and a translation vector, $\hat{t}$, by a quasi-Newton's method and project the result onto the space of Householder matrices using the Householder projection theorem.

Theorem 1:(Householder Projection Theorem) Let $A \in GL(3)$ be an affine matrix with negative determinant. The Householder reflection matrix, $\hat{H}$, which minimizes the Frobenius norm to A,

$$\hat{H} = \arg\min_H ||A - H||_F, \tag{4}$$

is given by:

$$\hat{H} = I - 2ee^T$$

where e is the eigenvector associated with the smallest eigenvalue of A.

Proof: From Equations (4) and (3) we obtain the following relation, which defines $\hat{H}$,

$$\hat{H} = ||A - (I - 2\hat{v}\hat{v}^T)||_F \text{ where}$$
$$\hat{v} = \arg\min_{\boldsymbol{v}} ||A - (I - 2vv^T)||_F.$$

where $||\cdot||_F$ denotes the Frobenius norm. Minimizing the second equation is equivalent to minimizing the following trace calculation

$$tr[(A - (I - 2vv^T))(A - (I - 2vv^T))^T] =$$
$$tr(AA^T) - 2tr(A) + 4tr(Avv^T) + 3.$$

Minimizing the above equation with respect to v reduces to the problem of minimizing $tr(Avv^T)$ with respect to v. Matrix A can be written with its eigendecomposition, $A = U\Sigma V^T$ where

$$\Sigma = \begin{bmatrix} \sigma_1 & 0 & 0 \\ 0 & \sigma_2 & 0 \\ 0 & 0 & \sigma_3 \end{bmatrix}, \sigma_1 \geq \sigma_2 \geq \sigma_3 \text{ and } V = [e_1\, e_2\, e_3].$$

Construct $v = V\alpha$ for some unit vector $\alpha = [\alpha_1, \alpha_2, \alpha_3]^T$. We then have

$$tr(Avv^T) = tr(U\Sigma V^T V\alpha\alpha^T V^T).$$

Since both U and V^T are orthogonal and thus do not contribute to the trace calculation we simply find a v that minimizes $tr(\Sigma\alpha\alpha^T)$. That is,

$$\hat{\alpha} = \arg\min_\alpha tr(\Sigma\alpha\alpha^T)$$
$$\arg\min_{\alpha_1,\alpha_2,\alpha_3} (\sigma_1\alpha_1^2 + \sigma_2\alpha_2^2 + \sigma_3\alpha_3^2)$$
$$\text{subject to : } \alpha_1^2 + \alpha_2^2 + \alpha_3^2 = 1.$$

This implies that $\hat{\alpha} = [0, 0, 1]^T$. Hence, $v = e_3$ the eigenvector associated with the smallest eigenvalue σ_3 of A. **QED.**

With the Householder Projection Theorem, we embed the optimization in $\mathbb{R}^{12}$ by first registering the image, $I(x)$, with it's reflection, $I_{re}(x)$, about the YZ-plane passing through the image centroid following Prima et al. [8]. Figure 2 exemplifies this procedure. In Figure 2, $I(x)$, a solid outline, is represented as an axial slice of a skull and $I_{re}(x)$, a dotted outline, as

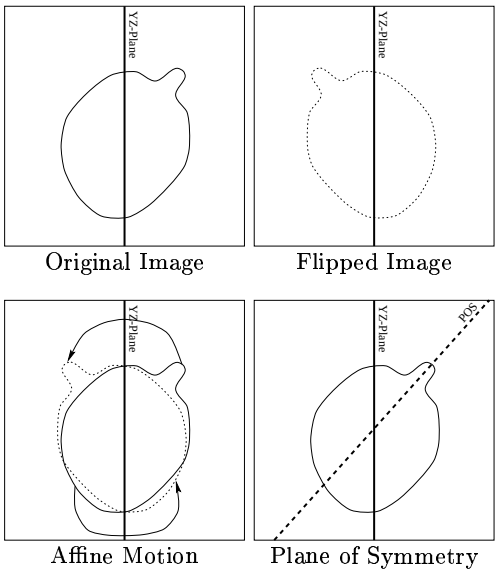

Fig. 2. The original image, the solid-line curve, is flipped about the YZ-plane to produce the dotted-line curve. The affine motion between these two images, shown by the arrows, is estimated from which the plane of symmetry, the vertical line, is produced.

a flipped version of the same. We define the reflected image, $I_{re}(x)$ via $I_{re}(x) = I(S(x-\mu)+\mu)$ where

$$S = \begin{bmatrix} -1 & 0 & 0 \\ 0 & 1 & 0 \\ 0 & 0 & 1 \end{bmatrix}$$

and μ is the centroid of $I(x)$. We estimate the $\hat{A}$, $\hat{t}$, and $\hat{f}$ according to

$$\hat{A},\hat{t},\hat{f} = \arg\min_{A,t,f} \int_\Omega ||I(x) - I_{re}(Ax+t) + f(x)||^2 dx + \beta \int_\Omega ||L_f f(x)||^2 dx. \quad (5)$$

The lower left panel of the figure illustrates the estimation of this affine motion, $\hat{A}$ and $\hat{t}$, via arrows that takes the original solid-line ellipse into the flipped dotted-line ellipse, such that $I_{re}(x) = I(\hat{A}(x-\mu)+\hat{t}+\mu)$. Reflecting $I_{re}(x)$ back across the YZ-plane produces $I(S\hat{A}(x-\mu)+\hat{t}+\mu)$ which best approximates the original image $I(x)$. The estimate of $\hat{H}$ then becomes the projection of $S\hat{A}$, which characterizes the normal, $\hat{v}$, in Equation (3) of the plane of symmetry. The estimate $\hat{q}$, which is the point in the point-normal representation of the plane, is given by solving the equation $-\hat{H}\hat{q}+\hat{q} = -\hat{H}\mu+\hat{t}+\mu$. Solving for $\hat{q}$ yields,

$$\hat{q} = \mu + (I-\hat{H})^{-1} \quad \text{and} \quad \hat{t} = \mu + \frac{1}{2} v v^T \hat{t}. \quad (6)$$

2.2 Quasi-Newton Optimization Algorithm

Having parameterized the plane of symmetry via the Householder matrix we now derive the Quasi-Newton optimization algorithm for estimating the affine motion, (A,t). Let $A^k = [a_{ij}^k]$, $t^k = [t_1^k, t_2^k, t_3^k]^T$ be the estimates after iteration k. The iterative algorithm is defined via the update step

$$A^{k+1} = A^k + \Delta A \quad \text{and} \quad t^{k+1} = t^k + \Delta t.$$

We prove that the estimates $(\hat{A},\hat{t})$ minimizing Equation (5) are given by the stable points of the algorithm. For convenience we define the notation,

$$X = \begin{bmatrix} \bar{x} & 0 & 0 & 1 & 0 & 0 \\ 0 & \bar{x} & 0 & 0 & 1 & 0 \\ 0 & 0 & \bar{x} & 0 & 0 & 1 \end{bmatrix}$$

, where $\bar{x} = [x_1, x_2, x_3]$ and

$$a^k = [\, a_{11}^k \; a_{12}^k \; a_{13}^k \; a_{21}^k \cdots \; t_1^k \; t_2^k \; t_3^k \,]^T.$$

Using the above notation, Equation (5) can be written as,

$$E(a^k) = \int_\Omega ||I(x) - I_{re}(Xa^k) + f^k(x)||^2 dx + \beta \int_\Omega ||L_f f^k(x)||^2 dx. \quad (7)$$

Let the estimate at iteration $k+1$, a^{k+1}, be given by the update $\Delta a \in \mathbb{R}^{12}$ of a^k, that is

$$a^{k+1} = a^k + \Delta a.$$

The energy in Equation (7) at iteration $k+1$ then becomes,

$$E(a^{k+1}) = \int_\Omega ||I(x) - I_{re}(X(a^k+\Delta a)) + f^k(x)||^2 dx + \beta \int_\Omega ||L_f \cdot f^k(x)||^2 dx.$$

Using the Taylor series expansion of $I_{re}(x)$ up to the second order about Xa^k, we approximate E^{k+1} as follows,

$$E(a^{k+1}) \approx \int_\Omega ||I(x) - [I_{re}(x) - \nabla I_{re}\,|_{Xa^k}^T (X\Delta a)] + f^k(x)||^2 dx + \beta \int_\Omega ||L_f f^k(x)||^2 dx \quad (8)$$

Notice that Equation (8) is quadratic with respect to Δa. The update step Δa is chosen to minimize $E(a^{k+1})$ which implies

$$\nabla_{\Delta a} E = 0.$$

Applying this gradient we obtain,

$$\begin{aligned}\nabla_{\Delta a} E &= \int_\Omega [I(x) - I_{re}(Xa^k) + f^k(x)]V(x)^T dx \\ &\quad + \left(\int_\Omega V(x)^T V(x) dx\right) \Delta a \\ &= 0\end{aligned}$$

where $V(x) = \nabla I_{re}|^T_{Xa^k} X$. Thus,

$$\begin{aligned}\Delta a = &- \left[\int_\Omega V(x)^T V(x) dx\right]^{-1} \times \\ &\int_\Omega [I(x) - I_{re}(Xa^k) + f^k(x)]V(x)^T dx \quad (9)\end{aligned}$$

Theorem 2: The stable points $\hat{a} = (\hat{A}, \hat{t})$ of the above iterative algorithm minimize the energy in Equation (5) and satisfy the necessary condition $\nabla_a E(\hat{a}) = 0$.

Proof: If $\hat{a}$ is a stable point of the above algorithm then the update Δa in Equation (9) is zero implying that

$$\int_\Omega [I(x) - I_{re}(Xa^k) + f^k(x)]V(x)^T dx = 0,$$

where, as before, $V(x) = \nabla I_{re}|^T_{Xa^k} X$. This is exactly the necessary condition for minimizer $\nabla_a E(\hat{a}) = 0$. **QED.**

After convergence of the algorithm we compute the estimate for the Householder reflection. From the Householder Projection Theorem and Equation (6) we have $\hat{H} = I - 2ee^T$ where e is the eigenvector associated with the smallest eigenvalue of $S\hat{A}$ and $\hat{q} = \mu + \frac{1}{2} ee^T \hat{t}$.

At each iteration of the Quasi Newton algorithm derived above for estimating (A, t), an estimate for the inter-hemispheric intensity variation $f^k(x)$ is obtained by minimizing

$$\begin{aligned}f^k &= \arg\min_f E(f) \\ &= \int_\Omega ||I(x) - I_{re}(A^k x + t^k) + f(x)||^2 dx \\ &\quad + \beta \int_\Omega ||L_f f(x)||^2 dx, \quad (10)\end{aligned}$$

where A^k, t^k are the estimates of the affine motion and $f^k(x)$ is the intensity field variation estimate at the k^{th} iteration. The necessary condition for the minimizer of (10) is that the Gateaux differential $\delta E(f; \eta)$ for all allowable perturbations η is zero [**?**]

$$\begin{aligned}&\delta E(f : \eta) \\ &= \frac{d}{d\alpha}[\int_\Omega ||I(x) - I_{re}(A^k x + t^k) + f^k(x) + \alpha\eta(x)||^2 dx \\ &\quad + \beta \int_\Omega ||L_f(f^k(x) + \alpha\eta(x))||^2 dx]|_{\alpha=0} dx \\ &= 2[\int_\Omega [I(x) - I_{re}(A^k x + t^k) + f^k(x)]\eta(x) dx \\ &\quad + \beta \int_\Omega L_f L_f^\dagger f^k(x) dx]\eta(x) dx\end{aligned}$$

where $L_f^\dagger$ is the adjoint of L_f. The conditions $\delta E(f; \eta) = 0$ for all $\eta(x)$ imply that $f^k(x)$ satisfy the differential equation,

$$I(x) - I_{re}(A^k x + t^k) + f(x) + \beta L_f L_f^\dagger f(x) = 0. \quad (11)$$

The above differential equation is solved using the Fast Fourier Transform as follows. Let Ω be a periodic discrete lattice having dimensions $L \times M \times N$. Further define the residue at iteration k to be $r^k(x) = [I_{re}(A^k x + t^k) - I(x)]$. Given this, the intensity differential equation (11) can be re-stated as,

$$[\beta L_f^+ L_f + 1] f^k(x) = r^k(x). \quad (12)$$

We write $f^k(x)$ and $r^k(x)$ in terms of their Fourier representations,

$$\begin{aligned}f^k(x) &= \sum_{w=0}^{N-1} \sum_{v=0}^{M-1} \sum_{u=0}^{L-1} F^k(u, v, w) e^{j\langle \omega, x\rangle} \\ r^k(x) &= \sum_{w=0}^{N-1} \sum_{v=0}^{M-1} \sum_{u=0}^{L-1} R^k(u, v, w) e^{j\langle \omega, x\rangle}\end{aligned}$$

where $\omega = [\omega_u, \omega_v, \omega_w]^T$ with $\omega_u = \frac{2\pi u}{L}, \omega_v = \frac{2\pi v}{M}, \omega_w = \frac{2\pi w}{N}$ and F^k, $R^k \in \mathbb{C}$. We re-write Equation (12) as,

$$Lf^k(x) = \sum_{w=0}^{N-1} \sum_{v=0}^{M-1} \sum_{u=0}^{L-1} L e^{j\langle \omega, x\rangle} F^k(u, v, w) \quad (13)$$

where $L = \beta L_f L_f^\dagger + 1$. As L is a differential operator with complex exponentials as it's eigenfunctions. Equation (13) becomes

$$Lf^k(x) = \sum_{w=0}^{N-1} \sum_{v=0}^{M-1} \sum_{u=0}^{L-1} \lambda(u, v, w) e^{j\langle \omega, x\rangle} F^k(u, v, w),$$

where $\lambda(u, v, w)$ are the eigenvalues of the operator L. We now compute the eigenvalues $\lambda(u, v, w)$:

$$\begin{aligned}\lambda(u, v, w) e^{j\langle \omega, x\rangle} &= L e^{j\langle \omega, x\rangle} \\ &= (\beta L_f L_f^\dagger + 1) e^{j\langle \omega, x\rangle} \quad (14) \\ &= (\beta \lambda_f^2(u, v, w) + 1) e^{j\langle \omega, x\rangle}\end{aligned}$$

where $\lambda_f(u,v,w)$ are the eigenvalues of the operator $L_f = \nabla^2$. Using the standard definition of the finite differences approximation of the Laplacian the eigenvalues become,

$$\lambda_f(u,v,w) = 2\cos\omega_u + 2\cos\omega_v + 2\cos\omega_w - 6.$$

Substituting the eigenvalues into (14) we obtain,

$$\lambda(u,v,w) = 4\beta[-6(\cos\omega_u + \cos\omega_v + \cos\omega_w) + 2(\cos\omega_u\cos\omega_v + \cos\omega_u\cos\omega_w + \cos\omega_v\cos\omega_w) + \cos^2\omega_u + \cos^2\omega_v + \cos^2\omega_w + 9] + 1.$$

Finally, we can compute $f(x)$ by taking the inverse Fast Fourier Transform,

$$f^{k+1}(x) = \frac{1}{2\pi LMN}\sum_{w=0}^{N-1}\sum_{v=0}^{M-1}\sum_{u=0}^{L-1}\frac{R^k(u,v,w)}{\lambda(u,v,w)}e^{-j\langle\omega,x\rangle}.$$

For an efficient implementation we employ a multi-scale approach in estimating $\hat{A}$ and $\hat{t}$ directly from $I(x)$. We construct a pyramid of three images of decreasing size taken at increasing scale via Gaussian kernel convolutions, $I(x;\sigma) = G(0,\sigma)\bigotimes I(x)$ where $\sigma = 2\tau$ and $\tau = 2, 4, 8$ voxels. The estimation process begins with the images at the largest scale by estimating $\hat{A}$ and $\hat{t}$ for the image. The results of this process become the initialization for the estimation process for the next smaller scale image. This process is repeated until $\hat{A}$ and $\hat{t}$ are estimated at the original scale of $I(x)$.

The convergence criteria for progress to successive scales is simply that both $||A^{k+1} - A^k|| < \varepsilon$ and $||t^{k+1} - t^k|| < \varepsilon$ for some sufficiently small ε.

An initial estimate for A^0 and t^0 is obtained via the method of moments as follows: define the first and the second moments of an image $I(x)$ as

$$\mu_I = \frac{1}{\int_\Omega I(x)dx}\int_\Omega xI(x)dx$$
$$K_I = \frac{1}{\int_\Omega I(x)dx}\int_\Omega (x-\mu_I)(x-\mu_I)^T I(x)dx$$

Notice that for an image $\tilde{I}(x) = I(Ax+t)$ the first and second moments of $\tilde{I}(x)$ can be expressed as

$$\mu_{\tilde{I}} = \mu_I - t \quad , \quad K_{\tilde{I}} = AK_IA^{-1}$$

Letting $S_1 = \sqrt{K_I}$ and $S_2 = \sqrt{K_{\tilde{I}}}$, it follows from the above equations that $A = S_1S_2^{-1}$ and $t = \mu_I - \mu_{\tilde{I}}$. Using this construction the initial estimates A^0 and t^0 are computed by calculating the first and second moments of the image $I(x)$ and it's reflected image $I_{re}(x)$.

2.3 Results

We have analyzed the performance of the plane of symmetry estimation algorithm on ten tumor patients. We have found that the plane of symmetry estimation algorithm to be visually robust in the presence of large tumors as well as to the original alignment of the plane of symmetry with respect to the YZ-plane. Figure (3) provides a validation test image of a patient which has been rotated axially twenty degrees. The image on the left shows the estimated plane of symmetry through an axial slice of data. The right side images shows a 3D iso-surface rendering of the same image with the estimated 3D plane of symmetry. Notice that the estimation of the plane of symmetry, also shown in magenta, is robust in the presence of the tumor.

Figure (4) shows the rate of convergence for the affine estimation portion of the algorithm for the taking an image (size of image) into a rotated version (axial rotation of thirty degrees) of the same. The left plot shows clearly the individual multi-scale stages. The plot on the right shows that the algorithm converges in approximately 500 seconds. The previous non-multi-scale implementation required substantially more time to converge.

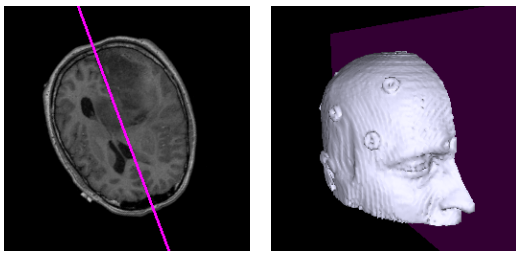

25 Degree Axial Rotation 3D Isosurface

Fig. 3. Shown on the left is an axial slice through a patient with the estimated plane of symmetry shown in purple. The right panel shows the 3D rendering of the skin as well as the estimated plane of symmetry. Notice the robustness of the algorithm in the presence of the large tumor.

3 Analysis of Inter-hemispheric Geometric Deformations via Image Mapping

After estimating the plane of symmetry, attention now focuses on small scale geometric differences across the plane of symmetry. The approach developed is similar to the work of Thirion et al. in that the

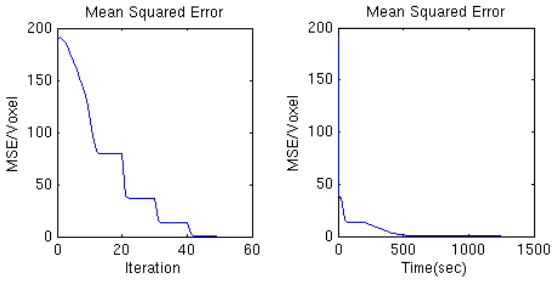

Fig. 4. Shown on the left is a per-iteration plot of the convergence of the estimation of the affine for an image with itself rotated by 30 degrees about the Z-axis. The right panel shows the same on a per-time basis.

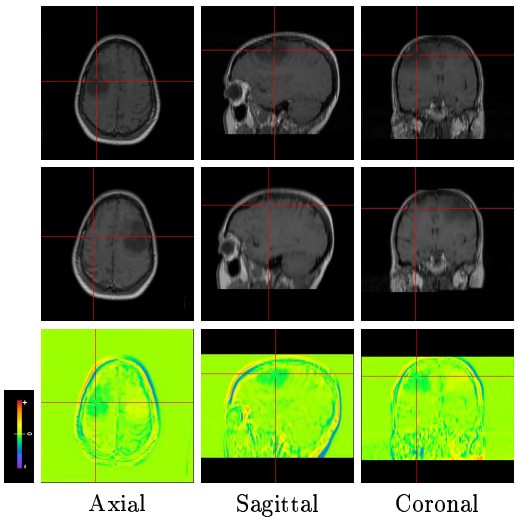

Fig. 5. The top row of the figure shows the axial sagittal and the coronal views through an example patient image with a glioma in the right frontal lobe. The middle row shows the same views of the image reflected about the plane of symmetry. The bottom row shows the difference between the original and reflected images.

geometric variation is captured via the definition of a high dimensional deformation field. However in previous work [23][24], such analyses have been directed purely toward detection of geometric differences. We present an algorithm that jointly estimates deformation and inter-hemispheric radiometric intensity differences. The method used for estimating the deformation field is an extension of the fluid flow formulation of Christensen et al. and is only briefly described here. For a complete description of the deformation algorithm see [14][15][?].

The high dimensional displacement vector field $d(x)$ and the scalar intensity field $f(x)$ are estimated using an alternating optimization technique that minimizes the quadratic error

$$\int_\Omega ||I(x) - I_{re}(H(x-q)+q+d(x)) + f(x)||^2 dx + \beta \int_\Omega ||L_f f(x)||^2 dx$$

where the $L_f = \nabla^2$ is a Laplacian operator that ensures smoothness of the estimate of $f(x)$ as in Equation 2 in the plane of symmetry estimation. Following Christensen, the deformation field $d(x)$ is defined via an integration of an O.D.E.

$$d(x) = x + \int_0^1 v(d(x,t),t)dt.$$

Energetics are induced on the velocity field $v(\cdot,t)$ using the Navier-Stokes operator $L_d = a\nabla^2 + b\nabla\cdot\nabla + cI$. The energetics induced on the velocity field become

$$E(v) = \int_0^1 \int_\Omega ||L_d v(x,t)||^2 dx dt.$$

Following [15], a computationally efficient algorithm for image matching is used which exploits the fact that the Navier-Stokes operator does not differentiate in time. A time indexed, $t_k, k = 1, \cdots, N$, sequence of optimizations are solved for a locally optimum velocity field $v(x,t_k)$. The transformation is then computed by forward integrating the locally optimum velocity field

$$d(x,t_{k+1}) = d(x,t_k) + \int_{t_k}^{t_{k+1}} v(d(x,\sigma),\sigma)d\sigma.$$

Since this is a locally-in-time optimal method the dimensionality of the optimization is reduced. The radiometric intensity variation is incorporated into this framework by performing the optimization for $f(x)$

at each time step

$$f^k(x) = \arg\min_f \int_\Omega ||I(x) - (I_{re}(H(x-q)+q+d(x,t_k))+ f(x)||^2 dx + \beta \int_\Omega ||L_f f(x)||^2 dx.$$

The above optimization is computed using the Fast Fourier Transform as described in section 2.2.

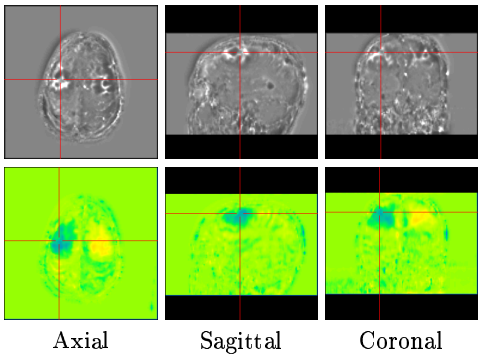

Fig. 6. The top row shows the same views through the determinant of the Jacobian of the transformation, . The bottom row shows the same views through the estimated intensity field capturing the inter-hemispheric radiometric differences.

3.1 Results

We have applied the above algorithms for the study of brain asymmetry in images of ten tumor patients. The top row of Figure (5) shows the axial, sagittal, and coronal views of a patient with an inter-hemispheric tumor mass. The plane of symmetry estimation algorithm was used to produce the reflected image across the plane of symmetry shown in the bottom row. The high dimensional deformation vector field, $d(x)$, capturing the normal and pathological inter-hemispheric geometric variability and the intensity field, $f(x)$, capturing the radiometric variation were calculated using the algorithm described above. In studying the inter-hemispheric geometric differences we calculate a modified Jacobian, $J(x)$, of the transformation $h(x) = x + d(x)$, The Jacobian of the deformation field captures the local inter-hemispheric volume differences of corresponding anatomical structures. Shown in the top row of Figure (6) is the Jacobian $J(h(x))$ where $J(h(x)) < 1$, light regions in the image, corresponds to contraction of volume and $J(h(x)) > 1$, dark regions in the image, which indicate dilation. The bottom row of Figure (6) shows the additive intensity image, $f(x)$, depicted in Figure (5) after 500 iterations of the algorithm.

4 Acknowledgments

The authors would like to thank Dr. Stephen Aylward of the department of radiology for his insightful suggestions and help during the development of this manuscript. We would also like to thank Nathan Moon for allowing us to use his image conversion utilities and Amy Chin Lorenzen for her assistance in editing the manuscript. The work was supported by NIH-NCI Grant R01 CA678

References

1. Wang, L., Joshi, S.C., Miller, M.I., Csernansky, J.G.: Statistical analysis of hippocampal asymmetry in schizophrenia. NeuroImage (2000)
2. Csernansky, J.G., Joshi, S.C., Wang, L., Miller, J.P., Miller, M.I.: Hippocampal morphometry in schizophrenia by high dimensional brain mapping. Volume 95. (1998) 11406–11411
3. Styner, M., Gerig, G.: Hybrid boundary-medial shape description for biologically variable shapes. In: Proceedings of IEEE Workshop on Mathematical Methods in Biomedical Image Analysis (MMBIA). (2000) 235–242
4. Styner, M., Gerig, G.: Medial models incorporating object variability for 3d shape analysis. In: Information Processing in Medical Imaging (IPMI). Lecture Notes in Computer Science (LNCS), Springer-Verlag (2001) 502–516
5. Hogan, R.E., Mark, K.E., Wang, L., Joshi, S., Miller, M.I., Bucholz, R.D.: Mr imaging deformation-based segmentation of the hippocampus in patients with mesial temporal sclerosis and temporal lobe epilepsy. Radiology **216** (2000) 291–297
6. Csernansky, J.G., Wang, L., Joshi, S., Miller, J., Gado, M., Kido, D., McKeel, D., Morris, J.C., Miller, M.I.: Early dat is distinguished from aging by high-dimensional mapping of the hippocampus. Neurology **55** (2000) 1636–1643
7. Thirion, J., Prima, S., Subsol, G.: Statistical analysis of dissymmetry in volumetric medical images. IEEE Workshop on Biomedical Image Analysis (1998) 74–83
8. Prima, S., Thirion, J., Subsol, G., Roberts, N.: Automatic analysis of normal dissymmetry of males and females in mr images. Proceedings of Medical Image Computing and Computer-Assisted Intervention (1998) 770–779
9. Sun, C., Sherrah, J.: 3d symmetry detection using the extended gaussian image. IEEE Transactions on Pattern Analysis and Machine Intelligence (PAMI) **19** (1997)

10. Moossy, J., Zubenko, G.S., Martinez, A.J., Rao, G.R.: Bilateral symmetry of morphologic lesions in alzheimer's disease. Archives of Neurology **45** (1988) 251–254
11. Smith, S., Jenkinson, M.: Accurate robust symmetry estimation. Proceedings of Medical Image Computing and Computer-Assisted Intervention (MICCAI) (1999) 308–317
12. Thompson, P.M., Moussai, J., Zohoori, S., Goldkorn, A., Khan, A.A., Mega, M.S., Small, G.W., Cummings, J.L., Toga, A.W.: Cortical variability and asymmetry in normal aging and alzheimer's disease. Cerebral Cortex **8** (1998) 492–509
13. Thompson, P.M., Mega, M.S., Vidal, C., Rapoport, J.L., Toga, A.W.: Detecting disease-specific patterns of brain structure using cortical pattern matching and a population-based probabilistic brain atlas. In: Proceedings of Information Processing in Medical Imaging (IPMI), Springer-Verlag (2001) 488–501
14. Christensen, G., Joshi, S., Miller, M.: Deformable templates using large deformation kniematics. IEEE Transactions on Medical Imaging **16** (1997) 864–877
15. Christensen, G.E., Rabbitt, R.D., Miller, M.I.: 3d brain mapping using a deformable neuroanatomy. Physics in Medicine and Biology **39** (1994) 209–618
16. Miller, M., Joshi, S., Christensen, G.: Large deformation fluid diffeomorphisms for landmark and image matching. In: Brain Warping. Wiley-Interscience (1999) 115–131
17. Talairach, J., Tournoux, P.: Co-Planar Stereotaxis Atlas of the Human Brain. Georg Thiem Verlag (1988)
18. Liu, Y.: Robust midsagittal plane extraction from course, pathological 3d images. Proceedings of Medical Image Computing and Computer-Assisted Intervention (2000)
19. Liu, Y., Collins, R.T., Rothfus, W.E.: Robust midsagittal plane extraction from normal and pathological 3-d neuroradiology images. IEEE Transactions on Medical Imaging (TMI) **20** (2001)
20. Ardekani, B.A., Kershaw, J., Braun, M., Kanno, I.: Automatic detection of the mid-sagittal plane in 3-d brain images. IEEE Transactions on Medical Imaging (TMI) **16** (1997)
21. Prima, S., Ourselin, S., Ayache, N.: Computation of the mid-sagittal plane in 3d medical images of the head. European Conference on Computer Vision (2000)
22. Joshi, S.C., Miller, M.I., Christensen, G.E., Banerjee, A., Coogan, T.A., Grenander, U.: Hierarchical brain mapping via a generalized dirichlet solution for mapping brain manifolds. In: Proc. of the SPIE's 1995 International Symposium on Optical Science, Engineering, and Instrumentation. Volume 2573. (August, 1995) 278–289
23. Davatzikos, C.: Spatial transformation and registration of brain images using elastically deformable models. Computer Vision and Image Understanding (CVIU) **66** (1997) 207–222
24. Gee, J.C., Bajcsy, R.K.: Elastic matching: Continuum mechanical and probabilistic analysis. In Toga, A.W., ed.: Brain Warping. Academic Press (1999)